

Prediction of a kagome topological superconducting family: XB_3 ($X = \text{Ni, Pd}$)Peng-Cheng Xiao ^{1,2}, Liu Yang,¹ Hong-Yan Lu ^{1,*}, Ning Hao ^{2,†} and Ping Zhang^{1,3,‡}¹*School of Physics and Physical Engineering, Qufu Normal University, Qufu 273165, China*²*Anhui Province Key Laboratory of Low-Energy Quantum Materials and Devices, High Magnetic Field Laboratory, HFIPS, Chinese Academy of Sciences, Hefei Anhui 230031, China*³*Institute of Applied Physics and Computational Mathematics, Beijing 100088, China*

(Received 7 November 2023; revised 25 January 2024; accepted 25 January 2024; published 12 February 2024)

Materials featuring the kagome configuration hold significant research potential following their discovery. Drawing inspiration from MgB_2 , we introduce a kagome topological superconducting family: XB_3 ($X = \text{Ni, Pd}$). This prediction is based on first-principles calculations and an analysis of bulk-edge correspondence. In this family, the boron atoms transition from their original honeycomb arrangement to form a stable kagome lattice, as confirmed by the phonon spectrum analysis. Through the calculations of the topological invariant and surface states, we establish that these materials belong to the \mathbb{Z}_2 Dirac metal category with nodal surface characteristics. Employing the Allen-Dynes modified McMillan formula, we anticipate superconducting critical temperatures, denoted as T_c , of 14.5 K for NiB_3 and 19.1 K for PdB_3 . These values surpass most of both conventional topological superconductors' candidates and kagome superconductors due to the relatively robust electron-phonon coupling. Moreover, the spin texture analysis of the Dirac cone at the high symmetry point K lends further support to their status as topological superconductors. Consequently, the XB_3 family presents an exciting platform for experimental investigations into topological superconductors and their potential applications in fault-tolerant quantum computation.

DOI: [10.1103/PhysRevB.109.054506](https://doi.org/10.1103/PhysRevB.109.054506)**I. INTRODUCTION**

The kagome lattice is distinguished by its unique electron band structures, encompassing Dirac fermions, flat bands, and van Hove singularities [1]. Among these, the linearly dispersed Dirac cones offer the possibility of nontrivial topology [2,3]. The minimal dispersion of the flat band leads to a prominent peak in the electronic density of states (DOS) [4,5], while the van Hove singularity presents a high density of divergent electron states [6,7], rendering it an ideal platform for realizing superconductors. Current research also highlights the significant potential of this material system in ordered states, such as charge density waves (CDW) [8–10], electronic nematicity [11–13], and pair density wave (PDW) [14]. The fundamental principles governing PDW formation remain elusive, with mutual coupling and competition observed among these different electron orders [1,11,15–17]. Furthermore, the kagome configuration's distinct geometric frustration forms the basis for investigations into quantum spin liquids [18,19] and contributes to the exploration of magnetic topological states [20], anomalous Hall effects [21,22], and chiral physics [23–26]. These areas undeniably represent focal points in the realms of condensed matter physics and materials physics. Therefore, it is of utmost importance to both theoretically predict and experimentally synthesize new

kagome materials while further exploring their potential for unconventional physical properties [27].

In the realm of known conventional BCS (Bardeen, Cooper, and Schrieffer) superconductors with topological properties, the superconducting transition temperature (T_c) is generally not high. Even in topological superconductors with kagome layers, T_c tends to hover below 10 K [16,28,29]. For example, within the AV_3Sb_5 ($A = \text{K, Rb, Cs}$) family, both CsV_3Sb_5 [30] and KV_3Sb_5 [31] are classified as \mathbb{Z}_2 topological metals, yet their T_c values are rather low at 2.5 K and 0.93 K, respectively [32]. In another family of topological superconductors, Ti_6X_4 ($X = \text{Bi, Sb, Pb, Tl, and In}$), T_c spans from 3.8 K to 5.1 K [33]. The relatively low T_c may pose great challenges in terms of material synthesis and practical applications. However, when we narrow our focus to the superconducting properties alone, the simple intercalated metal ion compound MgB_2 stands out with a high T_c of 39 K, approaching the McMillan limit [34]. This remarkable feature can be attributed to the triangular structure of the magnesium atomic layer, while the boron atomic layer exhibits a hexagonal honeycomb structure akin to graphene. These structural elements allow MgB_2 to maintain the record for the highest critical temperature under ambient pressure in phonon-mediated superconductors.

Building upon the previous research, this paper presents a theoretical prediction of a stable topological superconducting family, denoted as XB_3 ($X = \text{Ni, Pd}$). These materials share structural similarities with MgB_2 , with the notable difference being the transformation of the B layer from its hexagonal honeycomb arrangement to a kagome lattice. The elements

*hylyu@qfnu.edu.cn

†haon@hmfl.ac.cn

‡zhang_ping@iapcm.ac.cn

Ni and Pd reside within the tenth group of the Periodic Table. The introduction of the kagome layer gives rise to Dirac cones, safeguarded by lattice symmetry, in the vicinity of the Fermi level in reciprocal space. These cones feature nontrivial Fermi arcs on the material surfaces. In the absence of spin-orbit coupling (SOC), the system exhibits a class-I nodal surface [35]. Consequently, the nodal surface is perturbed once SOC is considered. The weak interlayer coupling in these materials allows for the concurrent analysis of spin textures in both bulk and surface states, further confirming their nontrivial topological properties [36]. Moreover, through first-principles calculations, it is established that these materials exhibit higher T_c in comparison to traditional topological superconductors candidates. Specifically, NiB₃ manifests a T_c of 14.5 K, while PdB₃ boasts a T_c of 19.1 K. This enhanced T_c is primarily attributed to the contribution of low-frequency vibration modes of X atoms to the electron-phonon coupling (EPC) within the system. The coexistence of superconductivity and nontrivial topological properties within the XB₃ family offers both theoretical and experimental guidance for further exploration of novel topological features in superconducting materials.

II. COMPUTATIONAL DETAILS

Our first-principles calculations, conducted within the framework of density functional theory (DFT) [37], were performed using three software packages: the QUANTUM-ESPRESSO (QE) package [38], the Vienna *ab initio* simulation package (VASP) [39], and the OPENMX package [40–43]. Electron- and phonon-related calculations within the DFT framework were carried out employing the Perdew-Burke-Ernzerhof parametrized generalized gradient approximation [44]. The interaction between ionic cores and valence electrons was represented using projector-augmented wave potentials in both the QE and VASP packages. Energy cutoffs of 100 Ry and 1000 Ry were set for the electronic wave functions within the plane-wave basis and for the charge density, respectively. The lattice parameters and atom positions were optimized through relaxation. The dynamical matrices and the EPC are calculated using density functional perturbation theory (DFPT) [45,46] within the linear response regime, providing input data for solving the isotropic Eliashberg equations. For phonon and EPC calculations, an $8 \times 8 \times 10$ q -point grid was employed based on the commutation relation between real and reciprocal lattice spaces. Furthermore, an accurate electron-phonon interaction matrix was evaluated using a denser $32 \times 32 \times 40$ k -point grid. In the OpenMX package, spin textures of bulk states were calculated for our study. We utilized pseudoatomic orbital basis sets, specifically (Ni6.0H-s3p2d1 and B7.0-s2p2d1) and (Pd7.0-s3p2d2 and B7.0-s2p2d1) for XB₃ ($X = \text{Ni, Pd}$), ensuring that they reproduce the electronic band structures calculated by VASP and QE. Surface states were determined using the iterative Green's function implemented in the WANNIERTOOLS package [47,48], with a basis set relying on maximally localized Wannier functions (MLWFs) [49,50] from the VASP2WANNIER90 interfaces [51]. This approach considered the $2p$ orbitals on B, $3d$ orbitals on Ni, and $4d$ orbitals on Pd.

Regarding the central formula, the total EPC constant λ was obtained via the isotropic Eliashberg function [52–54]:

$$\alpha^2 F(\omega) = \frac{1}{N(E_F)} \sum_{\mathbf{q}\nu} \delta(\omega - \omega_{\mathbf{q}\nu}) \frac{\gamma_{\mathbf{q}\nu}}{\omega_{\mathbf{q}\nu}}, \quad (1)$$

$$\lambda = 2 \int_0^\infty \frac{\alpha^2 F(\omega)}{\omega} d\omega. \quad (2)$$

Here, $\alpha^2 F(\omega)$ is the Eliashberg function, $N(E_F)$ is the DOS at the Fermi level, $\omega_{\mathbf{q}\nu}$ signifies the phonon frequency of the ν th phonon mode with wave vector \mathbf{q} , and $\gamma_{\mathbf{q}\nu}$ stands for the phonon linewidth [52–54]. The $\gamma_{\mathbf{q}\nu}$ can be estimated by

$$\gamma_{\mathbf{q}\nu} = \frac{2\pi\omega_{\mathbf{q}\nu}}{\Omega_{BZ}} \sum_{\mathbf{k},n,m} |g_{\mathbf{k}n,\mathbf{k}+\mathbf{q}m}^\nu|^2 \delta(\epsilon_{\mathbf{k}n} - E_F) \times \delta(\epsilon_{\mathbf{k}+\mathbf{q}m} - E_F). \quad (3)$$

In this equation, Ω_{BZ} represents the volume of the Brillouin zone (BZ), $\epsilon_{\mathbf{k}n}$ and $\epsilon_{\mathbf{k}+\mathbf{q}m}$ denote the Kohn-Sham energy, and $g_{\mathbf{k}n,\mathbf{k}+\mathbf{q}m}^\nu$ corresponds to the screened electron-phonon matrix element. The T_c value was estimated using the Allen-Dynes modified McMillan formula [54]:

$$T_c = \frac{\omega_{\log}}{1.2} \exp\left[\frac{-1.04(1 + \lambda)}{\lambda - \mu^*(1 + 0.62\lambda)}\right]. \quad (4)$$

The hysteretic Coulomb pseudopotential μ^* in Eq. (4) is set to 0.1 and the logarithmic average of the phonon frequencies ω_{\log} is defined as [54]

$$\omega_{\log} = \exp\left[\frac{2}{\lambda} \int \alpha^2 F(\omega) \frac{\log \omega}{\omega} d\omega\right]. \quad (5)$$

III. RESULTS AND DISCUSSIONS

A. Lattices structures and stability

The crystal structure of XB₃ ($X = \text{Ni, Pd}$) is depicted in Figs. 1(a) and 1(b). Its unit cell consists of two layers aligned along the c axis, with relatively weak interlayer interactions primarily governed by van der Waals forces. The B layer, serving as the kagome layer, is positioned in the middle of the structure, while X atoms are distributed at eight corners. In a top view, the arrangement of X atoms occupies the hollow sites of a hexagonal lattice formed by the B atoms. This crystal structure belongs to the $P6/mmm$ (No. 191) space group with inversion symmetry. In systems with inversion symmetry, utilizing the parity of wave functions to calculate the \mathbb{Z}_2 topological invariant is a more easily achievable method, as established in previous work [55,56]. The specific details will be discussed in the next section. Due to the rhombic shape of the unit cell's ab plane, the lattice constants a and b are identical. The specific values after full relaxation are listed in Table I. It is noteworthy that the real-space unit cell volume of PdB₃ is slightly larger than that of NiB₃, which can be attributed primarily to the larger atomic radius of Pd, as it occupies a position in the same group of the Periodic Table and is positioned below Ni.

To confirm the thermodynamic stability of this material family, the formation energy is calculated and defined as

$$E_f = \frac{E_{XB_3} - E_X - 3E_B}{4}, \quad (6)$$

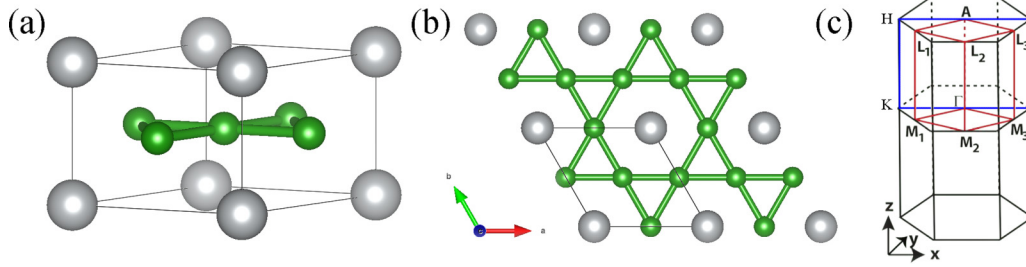


FIG. 1. Lattice structure (a), (b) and BZ (c) of XB_3 ($X = \text{Ni, Pd}$). (a) Side view; (b) top view. The silver spheres represent X atoms and the green spheres represent B atoms. (c) High-symmetry points and TRIMs are both marked on it. The region enclosed by the red lines and the eight TRIMs are used to define the topological index, while the area enclosed by the blue lines is used to visualize and project the 3D band structures.

where E_{XB_3} , E_X , and E_B represent the total energies of XB_3 ($X = \text{Ni, Pd}$), X , and B , respectively. In our calculations, we adopt space group $Fm\bar{3}m$ (No. 225) for Ni [57], space group $Fm\bar{3}m$ (No. 225) for Pd [57], and space group $R\bar{3}m$ (No. 166) for B [58]. As previously mentioned, all these structures are stable simple compounds that can naturally exist. As shown in the last column of Table I, the formation energies for both NiB_3 and PdB_3 are negative. These results strongly affirm their thermodynamic stability, indicating the feasibility of experimental synthesis, with the calculations serving as a valuable guideline for the experimental synthesis process. Additionally, the dynamic stability of this system is confirmed by the phonon spectrum (see Fig. 6), which exhibits no imaginary frequencies. Furthermore, theoretical calculations confirm that both materials are nonmagnetic substances [59], laying the foundation for their potential conventional superconducting properties.

B. Electronic and topological properties

In structures featuring the distinctive kagome pattern, the electronic structure and associated information serve as a crucial source of insight into their potential unique physical properties. Consequently, we have conducted calculations on the band structures and DOS in the vicinity of the Fermi level for this system, as depicted in Fig. 2. The band structures along the entire high-symmetry paths for both materials exhibit some similarities, particularly at the high-symmetry points K and H , where two Dirac-like crossing points are observed. Upon the inclusion of spin-orbit coupling (SOC), these four points exhibit band gap openings, although the degeneracy of each band is preserved. For NiB_3 , the gap sizes at the K and H points are 23.2 meV and 143.7 meV, respectively. In contrast, for PdB_3 , the corresponding values are 30.0 meV and 180.9 meV. Notably, the distinction between the two materials arises from the fact that, with an increase in

the atomic mass of X , the positions of the Dirac points shift upward and the gap values increase. These observations, in conjunction with the insights gained from the DOS, align with the characteristic features of kagome materials [60,61].

As shown in Fig. 3, our further calculations reveal the band structures along other high-symmetry lines, demonstrating that this system forms a continuous band that crosses the Fermi surface, connecting the two Dirac points along the K to H high-symmetry path. Intriguingly, with the introduction of the SOC effect, the entire band along this path opens a gap. To delve deeper into the analysis of its properties, we plot the 3D band structures in this region. When projected onto the k_x - k_z plane, it becomes evident that the previously mentioned continuous band effectively represents a nodal surface. Because it can be broken by SOC, it belongs to a class-I nodal surface [35,62–64]. Both materials are the same in this regard. Materials that exhibit ideal nodal surfaces are currently a rarity and our research presents possibilities for experimental exploration. Moreover, this system also exhibits nodal lines, indicative of its rich topological physical properties [64–67].

The eight points marked in Fig. 1(c) correspond to time-reversal invariant momentum points (TRIMs) in the reciprocal space of XB_3 ($X = \text{Ni, Pd}$); we can calculate the strong topological index ν_0 using the formula $(-1)^{\nu_0} = \prod_{i=1}^8 \delta(\Gamma_i)$, where $\delta(\Gamma_i)$ represents the product of parity eigenvalues of the occupied bands below the gap at the TRIM Γ_i [68–70].

Furthermore, the weak topological indices $\nu_{1,2,3}$ are defined as the products of parity eigenvalues at four TRIMs situated in a plane ($\mathbf{k}_{x,y,z} = \pi$) offset from the Γ point. Calculations based on the data in Table II reveal that both structures possess a \mathbb{Z}_2 index of (1; 000), signifying that $\nu_0 = 1$ and $\nu_1 = \nu_2 = \nu_3 = 0$. This unequivocally establishes that both materials qualify as strong topological materials.

In Fig. 4, we showcase the presence of nontrivial topological surface states on the (001) cleavage surface of the material. By analyzing their spin textures, we can observe that they are both the Rashba-like gapless topological surface states. When these two materials become superconductors below the critical temperature (T_c), the proximity effect of the bulk s -wave pairing to the Dirac-type surface states leads to an effective $p + ip$ topological superconductivity [71,72]. Nontrivial topological surface states on other surfaces are shown in Fig. 5, among which the Dirac-type surface states near the Fermi level are more conducive to realizing

TABLE I. Lattice parameters and formation energy of XB_3 ($X = \text{Ni, Pd}$).

	a (Å)	c (Å)	E_f (eV)
NiB_3	3.4938	2.8215	-1.2516
PdB_3	3.5066	3.3339	-0.5859

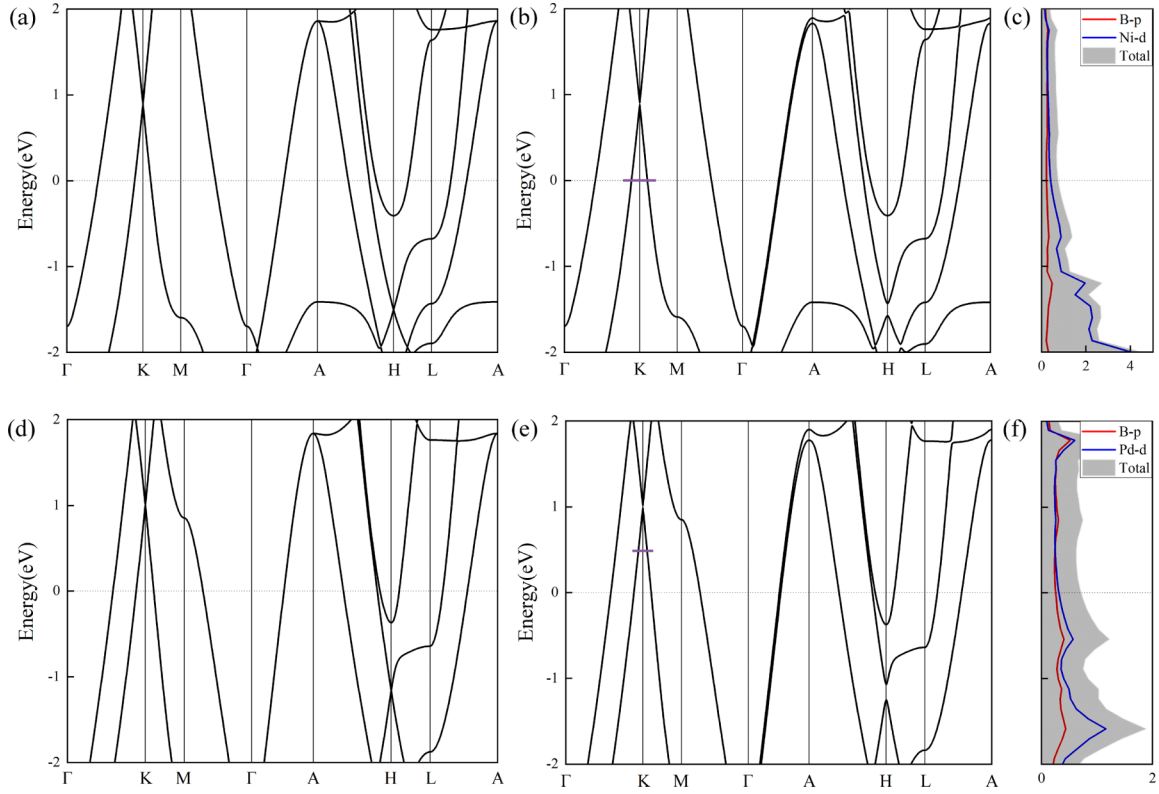


FIG. 2. Band structures and DOS near the Fermi level. Panels (a), (b), and (c) correspond to NiB_3 ; (d), (e), and (f) correspond to PdB_3 . Panels (a) and (d) do not consider SOC, while (b) and (e) take SOC into account. (c), (f) The shaded area in the graphs represents the total DOS, while the colored lines represent atomic orbitals-resolved DOSs. The purple short lines represent the positions for plotting the spin textures of the two materials in their respective bulk states.

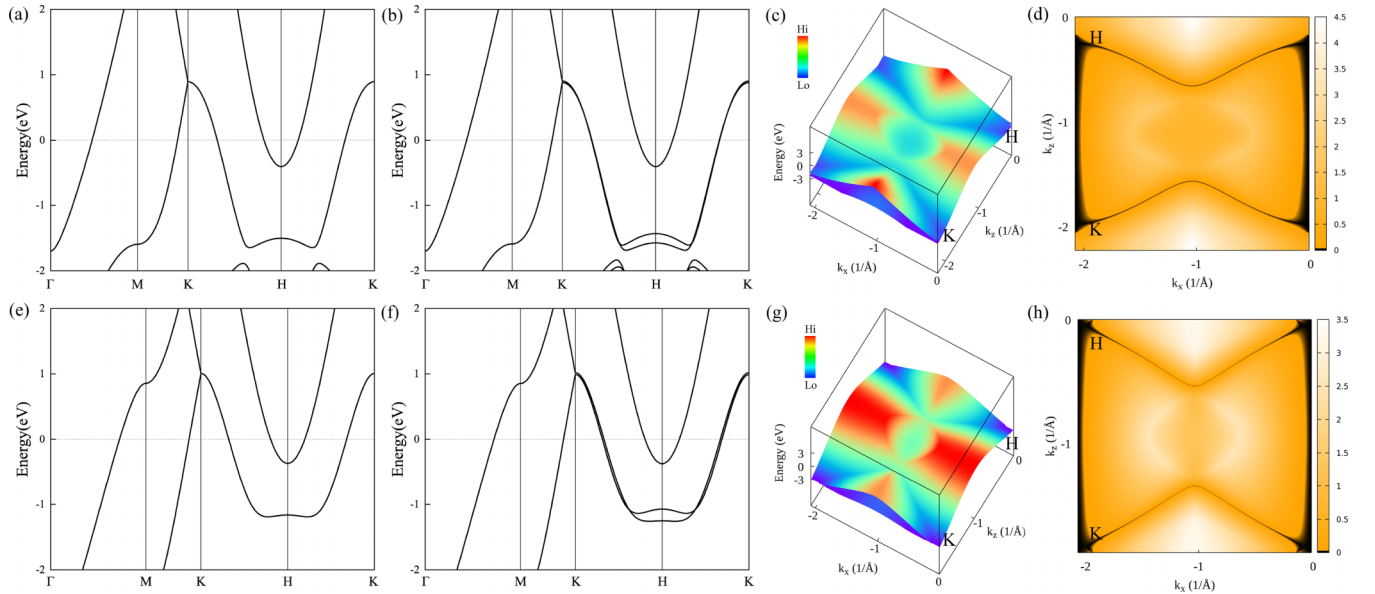


FIG. 3. Calculation and observation of nodal surface and nodal lines in XB_3 ($X = \text{Ni}, \text{Pd}$). The top and bottom panels represent NiB_3 and PdB_3 , respectively. Panels (a) and (e) are the band structures without considering SOC, while (b) and (f) take SOC into account. Panels (c) and (g) depict the 3D band structures of the eighth and ninth bands without considering SOC, while (d) and (h) show their projections onto the k_x - k_z plane. The black regions represent areas where the band gap is zero.

TABLE II. Parity eigenvalues of 10 occupied bands at eight TRIMs of XB_3 ($X = \text{Ni}, \text{Pd}$).

NiB_3		
TRIMs	Parities	Products
Γ	+1 -1 +1 -1 -1 +1 +1 +1 +1 -1	+1
M_1	-1 +1 +1 -1 +1 +1 +1 +1 +1 -1	-1
M_2	-1 +1 +1 -1 +1 +1 +1 +1 +1 -1	-1
M_3	-1 +1 +1 -1 +1 +1 +1 +1 +1 -1	-1
A	-1 +1 +1 +1 +1 +1 +1 +1 +1 +1	-1
L_1	+1 -1 -1 +1 +1 -1 +1 +1 +1 +1	-1
L_2	+1 -1 -1 +1 +1 -1 +1 +1 +1 +1	-1
L_3	+1 -1 -1 +1 +1 -1 +1 +1 +1 +1	-1
PdB_3		
TRIMs	Parities	Products
Γ	+1 -1 +1 +1 +1 -1 +1 +1 -1 -1	+1
M_1	-1 +1 +1 +1 -1 +1 +1 +1 +1 -1	-1
M_2	-1 +1 +1 +1 -1 +1 +1 +1 +1 -1	-1
M_3	-1 +1 +1 +1 -1 +1 +1 +1 +1 -1	-1
A	-1 +1 +1 +1 +1 +1 +1 +1 +1 +1	-1
L_1	+1 -1 +1 +1 -1 -1 +1 +1 +1 +1	-1
L_2	+1 -1 +1 +1 -1 -1 +1 +1 +1 +1	-1
L_3	+1 -1 +1 +1 -1 -1 +1 +1 +1 +1	-1

topological superconductivity. Therefore, after considering the SOC terms in the Dirac equation with linear dispersion, the results depicted in Figs. 4 and 5 hold paramount importance in confirming the topological superconducting nature of this system [29,36,73,74]. It is worth noting that when we project

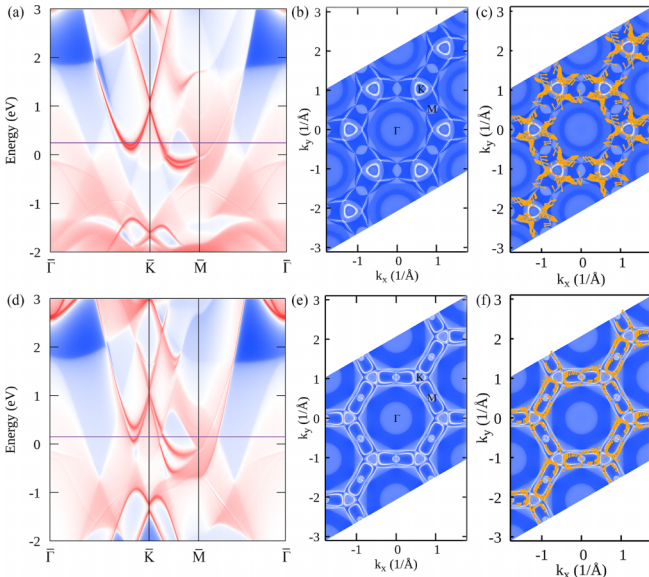


FIG. 4. Bright-colored red lines mean the topological surface states on the (001) surface of NiB_3 (a) and PdB_3 (d). The Fermi level is set to zero. The purple horizontal lines represent the chemical potentials at energy levels equivalent to +0.25 eV and +0.15 eV with respect to the Fermi level. Take k_x - k_y planes at these two positions to obtain (b) and (e). Panels (c) and (f) are the spin textures corresponding to (b) and (e). The orange arrows mean the directions of spin at topological surface states.

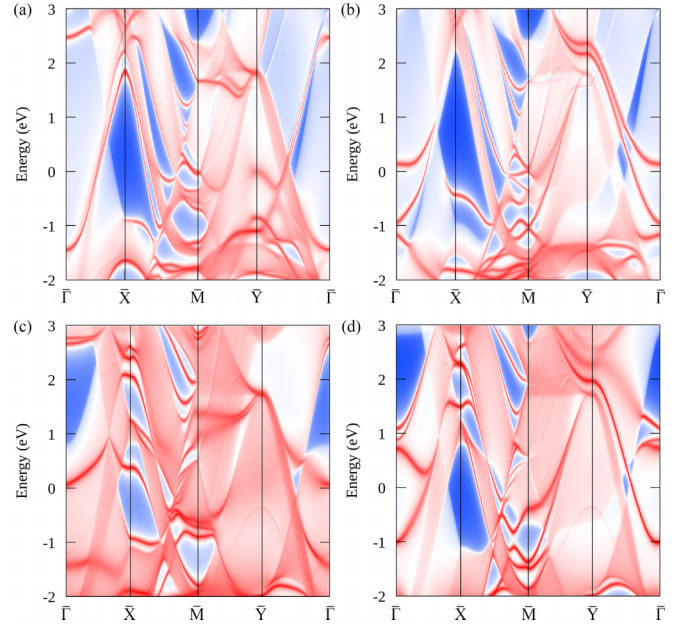


FIG. 5. Surface states in (a) (100) and (b) (010) planes for NiB_3 . (c), (d) The same as (a) and (b) but for PdB_3 . The Fermi level is set to zero.

the spin directions onto the two-dimensional k_x - k_y plane to create spin textures, any spin component along the s_z axis may lead to the spin directions not aligning perfectly with the shape of the energy states in the figure. However, this discrepancy does not affect the ultimate conclusions we draw.

C. Phonon vibrations and superconductivity properties

To better understand the characteristics of phonon vibrations and their interactions with electrons in XB_3 ($X = \text{Ni}, \text{Pd}$), we present the phonon spectra and phonon density of states in Fig. 6, taking into account contributions from different atomic vibration modes. In general, the phonon-related calculations do not include the SOC effects [75,76]. For these two materials, considering SOC, the relatively small gap opening in the band structures and the bands around the Fermi level remaining largely unchanged (see Sec. III B and Supplemental Material [77]) indicate a low strength of SOC. Therefore, the impact of SOC on describing vibrational properties is relatively minor. Due to variations in elemental masses, the vibration modes of X atoms primarily occupy the low-frequency region. Specifically, the vibrations of Ni atoms are observed at frequencies below 289 cm^{-1} , while the vibrations of Pd atoms occur at frequencies below 160 cm^{-1} . Moreover, X atoms with greater mass display more pronounced vibration modes that couple with the B atoms in the kagome layer. In the case of PdB_3 , a relatively flat and concentrated band emerges at a frequency of 128 cm^{-1} , corresponding to a prominent peak in the phonon density of states. This characteristic could contribute to enhanced EPC. However, there is limited coupling between in-plane (xy direction) and out-of-plane (z direction) vibrations of different atoms. Furthermore, some features on the phonon spectra resemble Dirac points observed in the band structure, which suggests the potential for investigating phonon topological properties in this material [78–80].

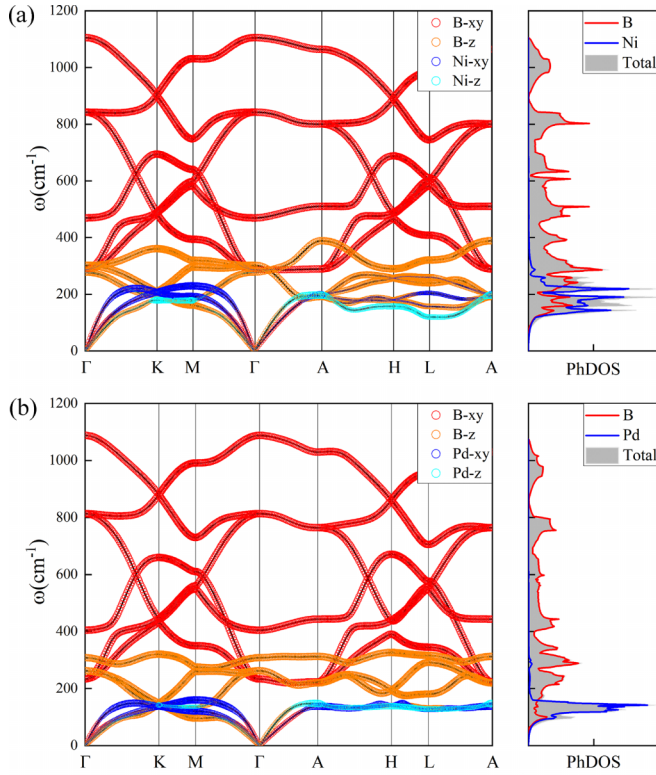


FIG. 6. Phonon dispersions weighted by different atomic vibrational modes as well as the total (gray-shaded zone) and atomic species-resolved (colored lines) phonon DOS of (a) NiB_3 and (b) PdB_3 .

Additionally, in Fig. 7, we present the phonon dispersions weighted by the magnitude of the linewidth $\lambda_{\mathbf{q}\nu}$, the Eliashberg electron-phonon spectral function $\alpha^2F(\omega)$, and the cumulative frequency dependence EPC constant λ . Here, $\lambda_{\mathbf{q}\nu}$ represents the EPC constant λ for the phonon mode $\mathbf{q}\nu$ [52–54], defined as

$$\lambda_{\mathbf{q}\nu} = \frac{\gamma_{\mathbf{q}\nu}}{\pi \hbar N(E_F) \omega_{\mathbf{q}\nu}^2}. \quad (7)$$

Clearly, the low-frequency vibrations of X atoms make a substantial contribution to the EPC. Our calculations yield λ values of 0.81 for NiB_3 and 1.15 for PdB_3 , corresponding to critical temperatures (T_c) of 14.5 K and 19.1 K, respectively. These relatively large EPC constants signify strong EPC characteristics. Quantitatively, the frequency range encompassing all Pd atoms' vibrations contributes approximately 44.3% to the total λ , while the frequency range encompassing all Ni atoms' vibrations contributes significantly, with a contribution of 72.8% to total λ .

By combining the phonon dispersions weighted by the magnitude of EPC $\lambda_{\mathbf{q}\nu}$ in Fig. 7 with those weighted by different atomic vibrational modes in Fig. 6, we observe that, in NiB_3 , the low-frequency out-of-plane vibrations of Ni atoms make the most substantial contribution, whereas in PdB_3 , it is the low-frequency out-of-plane vibrations of B atoms that dominate. This is because the proportion of different orbital contributions to the band structures near the Fermi level varies between the two materials. In NiB_3 , the d orbitals of Ni atoms

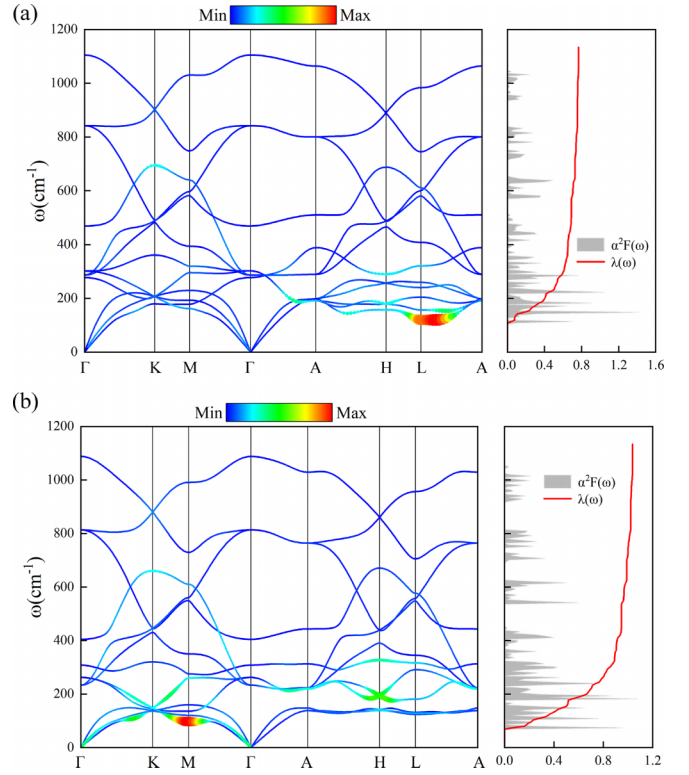


FIG. 7. (a) Phonon dispersions weighted by the magnitude of EPC $\lambda_{\mathbf{q}\nu}$ for NiB_3 . The right part displays the Eliashberg function $\alpha^2F(\omega)$ (shown as gray shading) and the integrated EPC strength of $\lambda(\omega)$ (indicated by the red line). (b) The same as (a), but for PdB_3 .

have a significantly higher contribution compared to the p orbitals of B atoms, especially at the L point. For PdB_3 , the contribution of the d orbitals of Pd atoms near the Fermi level is close to that of the p orbitals of B atoms, but at the M point, the p orbitals of B atoms completely dominate (see Supplemental Material [77]). These correspond precisely to the positions of the two extremities mentioned earlier. In summary, the introduction of X atoms may be one of the factors contributing to the higher T_c observed in this topological superconducting family.

IV. CONCLUSIONS

In conclusion, our first-principles calculations and analysis of bulk-edge correspondence have unveiled a kagome topological superconducting family, denoted as XB_3 ($X = \text{Ni}, \text{Pd}$), in this study. Our calculation results for formation energy and phonon dispersion confirm their thermodynamic and dynamic stability. Close to the Fermi level, Dirac cones emerge at the K and H points in the BZ, forming a nodal surface along the reciprocal space path from K to H . Upon the inclusion of the SOC effect, the Dirac points open gaps, resulting in the appearance of nontrivial surface states protected by topology. Moreover, this system exhibits strong EPC, with the out-of-plane and low-frequency vibration modes of the system's atoms making a substantial contribution to the EPC. Theoretically, our predicted topological superconducting family possesses a higher critical temperature (T_c) compared to other known conventional topological superconductors. We

strongly encourage experimental researchers to synthesize these materials and investigate the proposed phenomena, as this will establish a robust foundation for future fault-tolerant topological quantum computation.

ACKNOWLEDGMENTS

P.-C.X. thanks Q. Wang, X.-L. Huang, J.-Y. Li, Y.-H. Xiao, Y.-T. Shi, and Z.-W. Jing for helpful discussions. This work is supported by the National Natural Science Foundation of China (Grants No. 12074213 and No. 11574108), the Project of Introduction and Cultivation for Young Innovative

Talents in Colleges and Universities of Shandong Province, the National Key R&D Program of China (Grants No. 2022YFA1403200 and No. 2017YFA0303201), the National Natural Science Foundation of China (Grants No. 92265104, No. 12022413, and No. 11674331), the ‘‘Strategic Priority Research Program (B)’’ of the Chinese Academy of Sciences (Grant No. XDB33030100), the Major Basic Program of the National Science Foundation of Shandong Province (Grant No. ZR2021ZD01), the Basic Research Program of the Chinese Academy of Sciences Based on Major Scientific Infrastructures No. JZHKYPT-2021-08, and the CASHIPS Director’s Fund (Grant No. BJPY2023A09).

-
- [1] J.-X. Yin, B. Lian, and M. Z. Hasan, Topological kagome magnets and superconductors, *Nature (London)* **612**, 647 (2022).
- [2] H. Zhou, H. Liu, H. Ji, X. Li, S. Meng, and J.-T. Sun, Orbital degree of freedom induced multiple sets of second-order topological states in two-dimensional breathing Kagome crystals, *npj Quantum Mater.* **8**, 16 (2023).
- [3] H.-M. Guo and M. Franz, Topological insulator on the kagome lattice, *Phys. Rev. B* **80**, 113102 (2009).
- [4] Z. Jiang, Z. Liu, H. Ma *et al.*, Flat bands, non-trivial band topology and rotation symmetry breaking in layered kagome-lattice RbTi_3Bi_5 , *Nat. Commun.* **14**, 4892 (2023).
- [5] L. Huang and H. Lu, Protracted Kondo screening and kagome bands in the heavy-fermion metal Ce_3Al , *Phys. Rev. B* **102**, 155140 (2020).
- [6] Y. Luo, Y. Han, J. Liu *et al.*, A unique van Hove singularity in kagome superconductor $\text{CsV}_{3-x}\text{Ta}_x\text{Sb}_5$ with enhanced superconductivity, *Nat. Commun.* **14**, 3819 (2023).
- [7] B. Liu, M. Q. Kuang, Y. Luo, Y. Li, C. Hu, J. Liu, Q. Xiao, X. Zheng, L. Huai, S. Peng *et al.*, Tunable van Hove singularity without structural instability in kagome metal CsTi_3Bi_5 , *Phys. Rev. Lett.* **131**, 026701 (2023).
- [8] H. Li, G. Fabbris, A. H. Said *et al.*, Discovery of conjoined charge density waves in the kagome superconductor CsV_3Sb_5 , *Nat. Commun.* **13**, 6348 (2022).
- [9] H. Luo, Q. Gao, H. Liu *et al.*, Electronic nature of charge density wave and electron-phonon coupling in kagome superconductor KV_3Sb_5 , *Nat. Commun.* **13**, 273 (2022).
- [10] H. Li, T. T. Zhang, T. Yilmaz, Y. Y. Pai, C. E. Marvinney, A. Said, Q. W. Yin, C. S. Gong, Z. J. Tu, E. Vescovo, C. S. Nelson, R. G. Moore, S. Murakami, H. C. Lei, H. N. Lee, B. J. Lawrie, and H. Miao, Observation of unconventional charge density wave without acoustic phonon anomaly in kagome superconductors AV_3Sb_5 ($A = \text{Rb}, \text{Cs}$), *Phys. Rev. X* **11**, 031050 (2021).
- [11] L. Nie, K. Sun, W. Ma *et al.*, Charge-density-wave-driven electronic nematicity in a kagome superconductor, *Nature (London)* **604**, 59 (2022).
- [12] C. Mielke, D. Das, J.-X. Yin *et al.*, Time-reversal symmetry-breaking charge order in a kagome superconductor, *Nature (London)* **602**, 245 (2022).
- [13] T. Neupert, M. M. Denner, J.-X. Yin, R. Thomale, and M. Z. Hasan, Charge order and superconductivity in kagome materials, *Nat. Phys.* **18**, 137 (2022).
- [14] H. Chen, H. Yang, B. Hu *et al.*, Roton pair density wave in a strong-coupling kagome superconductor, *Nature (London)* **599**, 222 (2021).
- [15] S. Baidya, A. V. Mallik, S. Bhattacharjee, and T. Saha-Dasgupta, Interplay of magnetism and topological superconductivity in bilayer kagome metals, *Phys. Rev. Lett.* **125**, 026401 (2020).
- [16] X.-W. Yi, X.-Y. Ma, Z. Zhang, Z.-W. Liao, J.-Y. You, and G. Su, Large kagome family candidates with topological superconductivity and charge density waves, *Phys. Rev. B* **106**, L220505 (2022).
- [17] H. Zhao, H. Li, B. R. Ortiz, S. M. L. Teicher, T. Park, M. Ye, Z. Wang, L. Balents, S. D. Wilson, and I. Zeljkovic, Cascade of correlated electron states in the kagome superconductor CsV_3Sb_5 , *Nature (London)* **599**, 216 (2021).
- [18] C. Broholm, R. G. Cava, S. A. Kivelson, D. G. Nocera, M. R. Norman, and T. Senthil, Quantum spin liquids, *Science* **367**, eaay0668 (2020).
- [19] W. Zhu, X. Chen, Y.-C. He, and W. Witczak-Krempa, Entanglement signatures of emergent Dirac fermions: Kagome spin liquid and quantum criticality, *Sci. Adv.* **4**, eaat5535 (2018).
- [20] R. Chisnell, J. S. Helton, D. E. Freedman, D. K. Singh, R. I. Bewley, D. G. Nocera, and Y. S. Lee, Topological magnon bands in a kagome lattice ferromagnet, *Phys. Rev. Lett.* **115**, 147201 (2015).
- [21] Z. Zhang, J.-Y. You, X.-Y. Ma, B. Gu, and G. Su, Kagome quantum anomalous Hall effect with high Chern number and large band gap, *Phys. Rev. B* **103**, 014410 (2021).
- [22] E. Liu, Y. Sun, N. Kumar *et al.*, Giant anomalous Hall effect in a ferromagnetic kagome-lattice semimetal, *Nat. Phys.* **14**, 1125 (2018).
- [23] C. Guo, C. Putzke, S. Konyzheva *et al.*, Switchable chiral transport in charge-ordered kagome metal CsV_3Sb_5 , *Nature (London)* **611**, 461 (2022).
- [24] Y.-X. Jiang, J.-X. Yin, M. M. Denner *et al.*, Unconventional chiral charge order in kagome superconductor KV_3Sb_5 , *Nat. Mater.* **20**, 1353 (2021).
- [25] J. Zeng, Q. Li, X. Yang, D.-H. Xu, and R. Wang, Chiral-flux-phase-based topological superconductivity in kagome systems with mixed edge chiralities, *Phys. Rev. Lett.* **131**, 086601 (2023).
- [26] Z. Wang, Y.-X. Jiang, J.-X. Yin, Y. Li, G.-Y. Wang, H.-L. Huang, S. Shao, J. Liu, P. Zhu, N. Shumiya, M. S. Hossain, H. Liu, Y. Shi, J. Duan, X. Li, G. Chang, P. Dai, Z. Ye, G. Xu, Y. Wang *et al.*, Electronic nature of chiral charge order in the kagome superconductor CsV_3Sb_5 , *Phys. Rev. B* **104**, 075148 (2021).

- [27] M. Mandal, N. C. Drucker, P. Siriviboon *et al.*, Topological superconductors from a materials perspective, *Chem. Mater.* **35**, 6184 (2023).
- [28] J.-F. Zhang, P.-J. Guo, M. Gao, K. Liu, and Z.-Y. Lu, β -RhPb₂: A topological superconductor candidate, *Phys. Rev. B* **99**, 045110 (2019).
- [29] X.-H. Tu, P.-F. Liu, and B.-T. Wang, Topological and superconducting properties in YD₃ ($D = \text{In, Sn, Tl, Pd}$), *Phys. Rev. Mater.* **3**, 054202 (2019).
- [30] B. R. Ortiz, S. M. L. Teicher, Y. Hu, J. L. Zuo, P. M. Sarte, E. C. Schueller, A. M. M. Abeykoon, M. J. Krogstad, S. Rosenkranz, R. Osborn, R. Seshadri, L. Balents, J. He, and S. D. Wilson, CsV₃Sb₅: A \mathbb{Z}_2 Topological kagome metal with a superconducting ground state, *Phys. Rev. Lett.* **125**, 247002 (2020).
- [31] B. R. Ortiz, P. M. Sarte, E. M. Kenney, M. J. Graf, S. M. L. Teicher, R. Seshadri, and S. D. Wilson, Superconductivity in the \mathbb{Z}_2 kagome metal KV₃Sb₅, *Phys. Rev. Mater.* **5**, 034801 (2021).
- [32] B. R. Ortiz, L. C. Gomes, J. R. Morey, M. Winiarski, M. Bordelon, J. S. Mangum, I. W. H. Oswald, J. A. Rodriguez-Rivera, J. R. Neilson, S. D. Wilson, E. Ertekin, T. M. McQueen, and E. S. Toberer, New kagome prototype materials: discovery of KV₃Sb₅, RbV₃Sb₅, and CsV₃Sb₅, *Phys. Rev. Mater.* **3**, 094407 (2019).
- [33] X.-W. Yi, Z.-W. Liao, J.-Y. You, B. Gu, and G. Su, Topological superconductivity and large spin Hall effect in the kagome family Ti₆X₄ ($X = \text{Bi, Sb, Pb, Tl, and In}$), *iScience* **26**, 105813 (2023).
- [34] J. Nagamatsu, N. Nakagawa, T. Muranaka, Y. Zenitani, and J. Akimitsu, Superconductivity at 39 K in magnesium diboride, *Nature (London)* **410**, 63 (2001).
- [35] W. Wu, Y. Liu, S. Li, C. Zhong, Z. M. Yu, X. L. Sheng, Y. X. Zhao, and S. A. Yang, Nodal surface semimetals: Theory and material realization, *Phys. Rev. B* **97**, 115125 (2018).
- [36] Z. Wang, P. Zhang, G. Xu, L. K. Zeng, H. Miao, X. Xu, T. Qian, H. Weng, P. Richard, A. V. Fedorov, H. Ding, X. Dai, and Z. Fang, Topological nature of the FeSe_{0.5}Te_{0.5} superconductor, *Phys. Rev. B* **92**, 115119 (2015).
- [37] J. P. Perdew and A. Zunger, Self-interaction correction to density-functional approximations for many-electron systems, *Phys. Rev. B* **23**, 5048 (1981).
- [38] P. Giannozzi *et al.*, QUANTUM ESPRESSO: a modular and open-source software project for quantum simulations of materials, *J. Phys.: Condens. Matter* **21**, 395502 (2009).
- [39] G. Kresse and J. Furthmüller, Efficient iterative schemes for *ab initio* total-energy calculations using a plane-wave basis set, *Phys. Rev. B* **54**, 11169 (1996).
- [40] T. Ozaki, Variationally optimized atomic orbitals for large-scale electronic structures, *Phys. Rev. B* **67**, 155108 (2003).
- [41] T. Ozaki and H. Kino, Numerical atomic basis orbitals from H to Kr, *Phys. Rev. B* **69**, 195113 (2004).
- [42] T. Ozaki and H. Kino, Efficient projector expansion for the *ab initio* LCAO method, *Phys. Rev. B* **72**, 045121 (2005).
- [43] K. Lejaeghere *et al.*, Reproducibility in density functional theory calculations of solids, *Science* **351**, aad3000 (2016).
- [44] J. P. Perdew, K. Burke, and M. Ernzerhof, Generalized gradient approximation made simple, *Phys. Rev. Lett.* **77**, 3865 (1996).
- [45] S. Baroni, S. de Gironcoli, A. D. Corso, and P. Giannozzi, Phonons and related crystal properties from density-functional perturbation theory, *Rev. Mod. Phys.* **73**, 515 (2001).
- [46] D. M. Ceperley and B. J. Alder, Ground state of the electron gas by a stochastic method, *Phys. Rev. Lett.* **45**, 566 (1980).
- [47] Q. Wu, S. Zhang, H.-F. Song, M. Troyer, and A. A. Soluyanov, WannierTools: An open-source software package for novel topological materials, *Comput. Phys. Commun.* **224**, 405 (2018).
- [48] M. P. L. Sancho, J. M. L. Sancho, J. M. L. Sancho, and J. Rubio, Highly convergent schemes for the calculation of bulk and surface Green functions, *J. Phys. F: Met. Phys.* **15**, 851 (1985).
- [49] N. Marzari, A. A. Mostofi, J. R. Yates, I. Souza, and D. Vanderbilt, Maximally localized Wannier functions: Theory and applications, *Rev. Mod. Phys.* **84**, 1419 (2012).
- [50] I. Souza, N. Marzari, and D. Vanderbilt, Maximally localized Wannier functions for entangled energy bands, *Phys. Rev. B* **65**, 035109 (2001).
- [51] C. Franchini, R. Kováčik, M. Marsman, S. S. Murthy, J. He, C. Ederer, and G. Kresse, Maximally localized Wannier functions in LaMnO₃ within PBE + U , hybrid functionals and partially self-consistent GW: an efficient route to construct *ab initio* tight-binding parameters for e_g perovskites, *J. Phys.: Condens. Matter* **24**, 235602 (2012).
- [52] W. L. McMillan, Transition temperature of strong-coupled superconductors, *Phys. Rev.* **167**, 331 (1968).
- [53] R. C. Dynes, McMillan's equation and the T_c of superconductors, *Solid State Commun.* **10**, 615 (1972).
- [54] P. B. Allen and R. C. Dynes, Transition temperature of strong-coupled superconductors reanalyzed, *Phys. Rev. B* **12**, 905 (1975).
- [55] L. Fu, C. L. Kane, and E. J. Mele, Topological insulators in three dimensions, *Phys. Rev. Lett.* **98**, 106803 (2007).
- [56] L. Fu and C. L. Kane, Topological insulators with inversion symmetry, *Phys. Rev. B* **76**, 045302 (2007).
- [57] J. Häglund, A. Fernández Guillermet, G. Grimvall, and M. Körling, Theory of bonding in transition-metal carbides and nitrides, *Phys. Rev. B* **48**, 11685 (1993).
- [58] B. F. Decker and J. S. Kasper, The crystal structure of a simple rhombohedral form of boron, *Acta Crystallogr.* **12**, 503 (1959).
- [59] J. T. Haraldsen and R. S. Fishman, Spin rotation technique for non-collinear magnetic systems: application to the generalized Villain model, *J. Phys.: Condens. Matter* **21**, 216001 (2009).
- [60] G. Pokharel, S. M. L. Teicher, B. R. Ortiz, P. M. Sarte, G. Wu, S. Peng, J. He, R. Seshadri, and S. D. Wilson, Electronic properties of the topological kagome metals YV₆Sn₆, and GdV₆Sn₆, *Phys. Rev. B* **104**, 235139 (2021).
- [61] L.-T. Shi, J.-G. Si, A. Liang, R. Turnbull, P.-F. Liu, and B.-T. Wang, Topological and superconducting properties in bilayer kagome metals YT₆Sn₆ ($T = \text{V, Nb, Ta}$), *Phys. Rev. B* **107**, 184503 (2023).
- [62] C. Zhong, Y. Chen, Y. Xie, S. A. Yang, M. L. Cohen, and S. Zhang, Towards three-dimensional Weyl-surface semimetals in graphene networks, *Nanoscale* **8**, 7232 (2016).
- [63] Q. F. Liang, J. Zhou, R. Yu, Z. Wang, and H. M. Weng, Node-surface and node-line fermions from nonsymmorphic lattice symmetries, *Phys. Rev. B* **93**, 085427 (2016).
- [64] B.-B. Fu *et al.*, Dirac nodal surfaces and nodal lines in ZrSiS, *Sci. Adv.* **5**, eaau6459 (2019).
- [65] E. Cheng, W. Xia, X. Shi *et al.*, Pressure-induced superconductivity and topological phase transitions in the topological nodal-line semimetal SrAs₃, *npj Quantum Mater.* **5**, 38 (2020).

- [66] S.-Y. Xu *et al.*, Experimental discovery of a topological Weyl semimetal state in TaP, *Sci. Adv.* **1**, e1501092 (2015).
- [67] H. Weng, Y. Liang, Q. Xu, R. Yu, Z. Fang, X. Dai, and Y. Kawazoe, Topological node-line semimetal in three-dimensional graphene networks, *Phys. Rev. B* **92**, 045108 (2015).
- [68] H. Tan, Y. Liu, Z. Wang, and B. Yan, Charge density waves and electronic properties of superconducting kagome metals, *Phys. Rev. Lett.* **127**, 046401 (2021).
- [69] T. Machida, Y. Sun, S. Pyon, S. Takeda, Y. Kohsaka, T. Hanaguri, T. Sasagawa, and T. Tamegai, Zero-energy vortex bound state in the superconducting topological surface state of Fe(Se, Te), *Nat. Mater.* **18**, 811 (2019).
- [70] X.-H. Tu, P.-F. Liu, W. Yin, J.-R. Zhang, P. Zhang, and B.-T. Wang, Topological superconductivity in Rashba spin-orbital coupling suppressed monolayer β -Bi₂Pd, *Mater. Today Phys.* **24**, 100674 (2022).
- [71] X.-L. Qi, T. L. Hughes, S. Raghu, and S.-C. Zhang, Time-reversal-invariant topological superconductors and superfluids in two and three dimensions, *Phys. Rev. Lett.* **102**, 187001 (2009).
- [72] L. Fu and C. L. Kane, Superconducting proximity effect and majorana fermions at the surface of a topological insulator, *Phys. Rev. Lett.* **100**, 096407 (2008).
- [73] X.-L. Qi and S.-C. Zhang, Topological insulators and superconductors, *Rev. Mod. Phys.* **83**, 1057 (2011).
- [74] M. Sato and Y. Ando, Topological superconductors: a review, *Rep. Prog. Phys.* **80**, 076501 (2017).
- [75] B.-T. Wang, P. Zhang, R. Lizárraga, I. Di Marco, and O. Eriksson, Phonon spectrum, thermodynamic properties, and pressure-temperature phase diagram of uranium dioxide, *Phys. Rev. B* **88**, 104107 (2013).
- [76] L. Yan, B.-T. Wang, X. Huang, Q. Li, K. Xue, J. Zhang, W. Ren, and L. Zhou, Surface passivation induced a significant enhancement of superconductivity in layered two-dimensional MSi₂N₄ (M = Ta and Nb) materials, *Nanoscale* **13**, 18947 (2021).
- [77] See Supplemental Material at <http://link.aps.org/supplemental/10.1103/PhysRevB.109.054506> for orbital-resolved band structures and the global-opened band gap of XB₃ (X = Ni, Pd), and analysis of spin textures of the bulk states [81,82].
- [78] J. Li, J. Liu, S. A. Baronett, M. Liu, L. Wang, R. Li, Y. Chen, D. Li, Q. Zhu, and X.-Q. Chen, Computation and data driven discovery of topological phononic materials, *Nat. Commun.* **12**, 1204 (2021).
- [79] J. Gong, J. Wang, H. Yuan, Z. Zhang, W. Wang, and X. Wang, Dirac phonons in two-dimensional materials, *Phys. Rev. B* **106**, 214317 (2022).
- [80] G. Ding, C. Xie, J. Gong, J. Wang, J. Bai, W. Wang, D. Li, X.-P. Li, and X. Wang, Exotic topological phonon modes in semiconductors: Symmetry analysis and first-principles calculations for representative examples, *Phys. Rev. B* **108**, 075201 (2023).
- [81] H. Kotaka, F. Ishii, and M. Saito, Rashba effect on the structure of the Bi one-bilayer film: fully relativistic first-principles calculation, *Jpn. J. Appl. Phys.* **52**, 035204 (2013).
- [82] N. Yamaguchi and F. Ishii, Strain-induced large spin splitting and persistent spin helix at LaAlO₃/SrTiO₃ interface, *Appl. Phys. Express* **10**, 123003 (2017).